Aerospace Science and Technology 95 (2019) 105473

Contents lists available at ScienceDirect

Aerospace Science and Technology

www.elsevier.com/locate/aescte

The use of hybrid intuitive class shape transformation curves in aerodynamic design

Robert Christie *, Matthew Robinson, Fernando Tejero, David G. MacManus

Centre for Propulsion Engineering, School of Aerospace, Transport and Manufacturing, Cranfield University, Bedfordshire MK43 0AL, United Kingdom of Great Britain and Northern Ireland

ARTICLE INFO

Article history:
Received 27 February 2019
Received in revised form 1 October 2019
Accepted 9 October 2019
Available online 23 October 2019

Keywords:
Class shape transformation curves
Parametric design
Civil intakes
Fan cowl design
Turbofan engine aerodynamics
Computational fluid dynamics

ABSTRACT

The inherent mathematical smoothness of intuitive class shape transformation (iCST) curves has been shown to be suitable for the design of aerodynamic shapes. However, this property means that any changes to a constraint are not local but will result in a modification to the whole curve. This poses a problem to the aerodynamic designer when different parts of the curve are required to fulfil particular design requirements. A Hybrid iCST (HiCST) parameterisation approach is proposed which allows two sections of a single aero-line curve to be decoupled, without geometric discontinuity, whilst maintaining the dimensionality of a design problem. The HiCST approach has been tested on two key aerodynamic components of an aero-engine. Firstly, a design space exploration and optimisation were carried out for an aero-engine fan cowl. A comparison of Pareto fronts showed a 3.9% reduction in the minimum achievable nacelle drag from the iCST to the HiCST parameterisation. Secondly, aero-engine intakes were designed with both the iCST and HiCST parameterisations. The HiCST intake showed improved aerodynamic performance in terms of DC_{60} and IPR and proved more insensitive to changes in massflow and incidence. This development of the method for an aero-engine fan cowl and intake highlights the potential aerodynamic benefit from the proposed HiCST method.

© 2019 The Authors. Published by Elsevier Masson SAS. This is an open access article under the CC BY license (http://creativecommons.org/licenses/by/4.0/).

1. Introduction

Aerodynamic shapes can be represented in a number of ways. The most basic approach is to construct the shape from a point cloud of co-ordinates. This method requires a large number of design variables to guarantee a smooth and accurate shape [1]. Other parameterisation approaches range from general mathematical descriptions of curves and surfaces including B-splines [2], Bézier curves [3], Non-Uniform Rational B-splines (NURBS) [4,5], as well as methods developed particularly for aerodynamic shapes such as Hicks-Henne Bump functions [6,7], the PARSEC method [8], and the Class-Shape-Transformation (CST) approach [9–12]. An alternative approach is free-form deformation (FFD) [13] which allows smooth global deformations of the reference shape and can reduce the overall number of design variables [14].

The choice of parameterisation method has a profound effect on the design space and is a key decision in the design process [15]. Two key considerations for the aerodynamic designer are the number of and intuitiveness of the design variables. The PARSEC parameterisation method is an aerodynamically intuitive approach however it is unable to provide the required flexibility for airfoil design [16]. It is unable to provide high flexibility because it fails in the inverse design for some airfoils [17].

Bézier curves have control points which are only indirectly related to resultant aerodynamic performance [18]. A combined Bézier-PARSEC parameterisation was developed which combines the advantages of the Bézier approach with the more aerodynamically oriented parameters of the PARSEC method [18]. CST curves are known from wing profile design to create aerodynamically useful shapes [9,10]. This method is capable of producing a wide range of aerodynamic shapes in a universal way with a small number of design variables [9] including turbofan exhausts [19], helicopter blade profiles [20,21], aircraft bodies [22–24], mail slot intake-nozzle nacelles [25] and fan blade geometric perturbations [26]. The CST method uses a relatively small number of design variables but similarly to Bézier curve methods the requirement for the design parameters to be physically intuitive to a designer is not met [16].

The PARSEC [8] parameterisation was previously combined with the highly flexible CST parameterisation method [16]. This intuitive CST (iCST) approach is a transformation of the CST parameterisation method to a full set of intuitive parameters by a transformation matrix [16]. The iCST approach has been generalised to

* Corresponding author.
E-mail address: r.christie@cranfield.ac.uk (R. Christie).

https://doi.org/10.1016/j.ast.2019.105473
1270-9638/© 2019 The Authors. Published by Elsevier Masson SAS. This is an open access article under the CC BY license (http://creativecommons.org/licenses/by/4.0/).

a system which analytically calculates the transformation matrix for a set of arbitrary constraints [27,28]. iCST curves have been shown to be suitable for the design of aerodynamic shapes due to their mathematical smoothness [28]. However, any change to a curve parameter has an effect on the entire curve [29]. It may be that different parts of the curve that defined the aerodynamic cure (aero-line) are required to fulfil different design requirements. In this case the use of a single iCST curve will lead to a compromise between the different design requirements. One approach to overcome this limitation is to decouple parts of an iCST curve through the use of multiple intersecting iCST curves. The level of geometric continuity at the intersections can be controlled by specifying a derivative constraint of the requisite order. This decoupling can be achieved without additional user constraints or increasing the order of the parameterisation. In the current work these intersecting iCST curves are termed Hybrid iCSTs (HiCSTs).

The aerodynamic benefit of constructing an aero-engine fan cowl and an intake with a HiCST as opposed to an iCST parameterisation is investigated. Nacelle drag characteristics are investigated through 2D axisymmetric Computational Fluid Dynamics (CFD), while the intake aerodynamic performance is assessed with 3D CFD. These aerodynamic components have been chosen because they represent challenging aerodynamic design problems with conflicting design requirements due to the range of underlying flow mechanisms and the range of operating conditions.

2. Methodology

2.1. CST curves

A CST curve is formed by the product of a Class Function ($C(\psi)$) and a Shape Function ($S(\psi)$) plus a parameter ($\Delta\xi_{te}$) which controls the trailing point offset as follows,

$$\xi(\psi) = S(\psi)C(\psi) + \psi\,\Delta\xi_{te} \;\; ; \;\; \xi = \frac{y}{c} \;\; , \;\; \psi = \frac{x}{c} \tag{1}$$

where c is the curve length in the x-direction [9,10]. The Class Function is chosen to be geometrically similar to the final CST shape. The shape function comprises a set of Bernstein Polynomials. These polynomials form a partition of unity and as such by applying a coefficient to each polynomial the resultant CST shape can be controlled. Bernstein Polynomials also have infinitely continuous derivatives [9]. Therefore when a mathematically smooth Class Function is chosen, the CST curve is also mathematically smooth. This property of CST curves has been shown to be suitable for the design of aerodynamic shapes [28]. An example of such a class function which describes basic external aerodynamic shapes through different exponent combinations takes the form [9]:

$$C^{N_1}_{N_2}(\psi) = \psi^{N_1}[1-\psi]^{N_2} \;\text{ for }\; 0 \le \psi \le 1 \tag{2}$$

The exponents (N_1 and N_2) in Equation (2) can be altered to create a range of aerodynamic shapes including, Sears Hack ($C^{0.75}_{0.75}$), cone ($C^{0.+}_{1.0}$), biconvex ($C^{1.0}_{1.0}$), elliptic ($C^{0.5}_{0.5}$) and a round nosed airfoil ($C^{0.5}_{1.0}$). This last Class Function ($C^{0.5}_{1.0}$) is commonly used to describe wing sections, aero-engine intakes and fan-cowls [28]. When this Class Function is employed the first and nth Bernstein Polynomial Coefficients can be analytically calculated from the constraints applied to the CST curve (Eq. (3)). Unlike other Bernstein Polynomial coefficients they are not a function of other Bernstein Polynomial coefficients. The 0th and nth Bernstein Polynomial Coefficients are defined as,

$$bp_0 = \sqrt{\frac{2R_{le}}{c}} \;\; ; \;\; bp_n = \tan(\beta) + \frac{\delta z_{te}}{c} \tag{3}$$

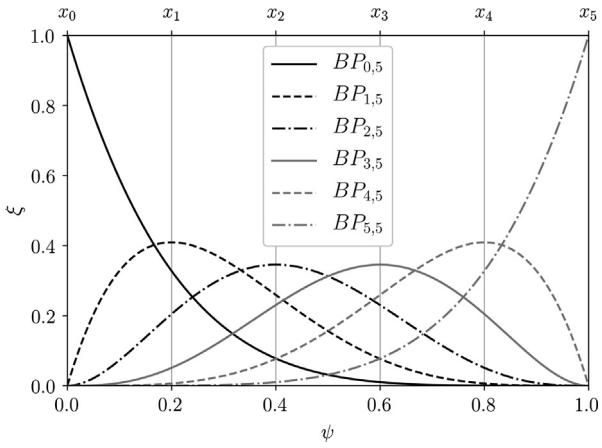


Fig. 1. 5th order Bernstein Polynomials.

where R_{le} is the radius of curvature at $\phi = 0$ and $\tan\beta$ is the gradient at $\phi = 1$ and [9].

2.2. iCST curves

Modifying CST shapes by manipulating the Bernstein Polynomial coefficients is non-intuitive to the aerodynamic designer, with no obvious link to familiar aerodynamic or geometric parameters. This drawback of CST curves has been addressed by the development of iCST curves [16,28]. The iCST method allows the analytical calculation of the Bernstein Polynomial coefficients as a function of any constraints imposed by the designer. These constraints can take the form of a positional hard-point through which the curve must pass or an imposed nth derivative at a specified ordinate. A linear set of equations (Eq. (4)) can be constructed,

$$\mathbf{A}\cdot\mathbf{X} = \mathbf{B} \tag{4}$$

where **A**, **B** and **X** are the matrices of coefficients, constant terms and solutions respectively. For every geometrical constraint imposed upon the curve an equation is added to the linear set of equations (Eq. (4)) which relates the constraint to the Bernstein Polynomial coefficients through Equation (5) [28].

$$\xi^{(k)}(\psi) = \left[\sum_{i=0}^{N}\left[bp_i K_{i,n}\left(\psi^i(1-\psi)^{n-i}\right)\right]C(\psi) + \psi\,\Delta\xi_{te}\right]^{(k)} \tag{5}$$

The shape function and its derivatives can be solved by using the fact that derivatives of the kth degree Bernstein Polynomials are polynomials of degree $k-1$ and can be written as a linear combination of Bernstein Polynomials (Eq. (6)) [28]. The solution of Equation (5) is then straightforward and Equation (4) can then be inverted (Eq. (7)) to solve for the Bernstein Polynomial coefficients.

$$\frac{d}{d\psi}BP_{i,n}(\psi) = n[BP_{k-1,n-1}(\psi) - BP_{k,n-1}(\psi)] \tag{6}$$

$$\mathbf{X} = \mathbf{A}^{-1}\cdot\mathbf{B} \tag{7}$$

2.3. Hybrid iCST methodology

The mathematically smooth nature of iCST curves has be shown to be suitable for the design of aerodynamic shapes [28]. A major consequence of this property is that the whole curve is altered by changes to a constraint. The contribution of each Bernstein Polynomial to the Shape Function is shown in Fig. 1. The control points, x_i, the abscissae of the maximum of the ith Bernstein Polynomial [29] are highlighted. The ith control point is the point of maximum

Table 1
Constraints for an example iCST parameterisation and equivalent HiCST of the same order with rate of change of curvature continuity at the intersection point. The HiCST is composed of two curves, a forebody curve ($HiCST_A$) and an afterbody curve ($HiCST_B$)).

#	Type	ψ	iCST $\xi^{(k)}(\psi)$	HiCST$_A$ $\xi^{(k)}(\psi)$	HiCST$_B$ $\xi^{(k)}(\psi)$
C.1	Position	0.0	$\xi\|_{\psi=0.0}$	$\xi\|_{\psi=0.0}$	$\xi\|_{\psi=0.0}$
C.2	Position	1.0	$\xi\|_{\psi=1.0}$	$\xi\|_{\psi=1.0}$	$\xi\|_{\psi=1.0}$
C.3	R	0.0	R$\|_{\psi=0.0}$	R$\|_{\psi=0.0}$	R$\|_{\psi=0.0}$
C.4	Position	ψ_{int}	$\xi\|_{\psi_{int}}$	$\xi\|_{\psi_{int}}$	$\xi\|_{\psi_{int}}$
C.5	Gradient	ψ_{int}	0.0	0.0	0.0
C.6	2nd derivative	ψ_{int}	n/a	n/a	$\xi_A^{(2)}\|_{\psi_{int}}$
C.7	3rd derivative	ψ_{int}	n/a	n/a	$\xi_A^{(3)}\|_{\psi_{int}}$
C.8	2nd derivative	1.0	$\xi^{(2)}\|_{\psi=1.0}$	n/a	$\xi^{(2)}\|_{\psi=1.0}$
C.9	Gradient	1.0	$\xi^{(1)}\|_{\psi=1.0}$	$\xi^{(1)}\|_{\psi=1.0}$	$\xi^{(1)}\|_{\psi=1.0}$

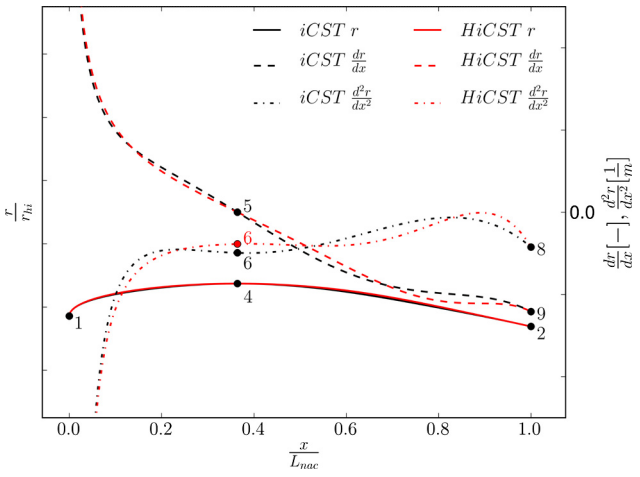


Fig. 2. Geometry, first and second order spatial derivatives of r w.r.t. to x and the imposed constraints for Fan Cowl A (iCST) and Fan Cowl B (HiCST). (For interpretation of the colours in the figure(s), the reader is referred to the web version of this article.)

influence for the ith Bernstein Polynomial. The 0th and nth Bernstein Polynomials are the only polynomials to influence the 0th and nth control points respectively. All other control points are influenced by all n Bernstein Polynomials. The consequence of this to an aero-line designer is that a modification of any iCST constraint will modify the whole curve. No part of the curve can be designed in isolation.

In some cases the use of a single iCST curve will lead to a compromise between the different design requirements. For example, an intake designer may design an intake lip to control local flow acceleration and an intake diffuser to control flow diffusion [28]. If this intake is constructed with a single iCST curve then a trade-off will have to be made between the lip and diffuser aerodynamic performance. An alternative approach which used multiple, intersecting iCST curves would decouple the curve at the intersection points. This decoupling can be achieved without additional constraints or an increase in the order of the parameterisation. The level of geometric continuity at the intersection can be controlled by specifying a derivative constraint of the requisite order. In this work these intersecting iCST curves are termed HiCSTs.

To illustrate the HiCST approach the constraints for a previously employed fan-cowl iCST parameterisation [30,31] and equivalent HiCST of the same order with rate of change of curvature continuity at the intersection point are given in Table 1 and Fig. 2. This parameterisation uses the round nosed, sharp trailing edge airfoil Class Function ($C_{0.5}^{1.0}$). If more precise control of the geometry is required further positional and derivative constraints can be imposed. The radius of curvature, (R), is specified at the leading edge, a local maximum is imposed and a gradient and 2nd derivative is specified at the trailing edge. Outlined here is the methodology to calculate the 4 Bernstein Polynomial coefficients for the iCST aero-line. For this Class Function, ($C_{0.5}^{1.0}$), the first and fourth Bernstein Polynomial coefficients for the iCST aero-line can be calculated with Equation (3). Equation (3), in conjunction with the constraints $C.3$ and $C.9$ (Table 1) can be rewritten as Equation (8).

$$bp_0 = \sqrt{2R|_{\psi=0.0}} \;;\; bp_4 = \xi^{(1)}|_{\psi=1.0} + \xi|_{\psi=1.0} - \xi|_{\psi=0.0} \tag{8}$$

The remaining three Bernstein Polynomial coefficients depend on constraints $C.4$, $C.5$ and $C.8$ and can be calculated with Equation (7). **A** is the matrix of coefficients and is given by:

$$\mathbf{A} = \begin{bmatrix} a_{1,1} & a_{1,2} & a_{1,3} \\ a_{2,1} & a_{2,2} & a_{2,3} \\ a_{3,1} & a_{3,2} & a_{3,3} \end{bmatrix} \tag{9}$$

B is the matrix of constants which is defined as:

$$\mathbf{B} = \begin{bmatrix} b_{1,0} & b_{2,0} & b_{3,0} \end{bmatrix}^T \tag{10}$$

Finally **X** is the matrix of Bernstein Polynomial coefficients:

$$\mathbf{X} = \begin{bmatrix} bp_1 & bp_2 & bp_3 \end{bmatrix}^T \tag{11}$$

Constraint C.4 (Table 1) is a positional constraint, therefore $k = 0$ and Eq. (5) can be rearranged to isolate the function coefficients and constant terms as given by Eq. (12) and Eq. (13) respectively.

$$a_{1,n} = [BP_{1,n} + BP_{2,n} \ldots + BP_{n-1,n}]C(\psi) \tag{12}$$

$$b_{1,0} = \xi - A_0 BP_{0,n} C(\psi) - A_n BP_{n,n} C(\psi) - \psi \Delta\xi_{te} \tag{13}$$

$k = 1$ for constraint C.5 (Table 1) as it is a first derivative constraint. The coefficients and constant terms in Eq. (5) are given by Eq. (14) and Eq. (15).

$$a_{2,n} = [BP_{1,n} + BP_{2,n} \ldots + BP_{n-1,n}]'C(\psi) + [BP_{1,n} + BP_{2,n} \ldots + BP_{n-1,n}]C'(\psi) \tag{14}$$

$$b_{2,0} = \xi'(\psi) - \Delta\xi_{te} - A_0 BP_{0,n} C'(\psi) - A_n BP_{n,n} C'\psi - A_0 BP'_{0,n} C_\psi - A_n BP'_{n,n} C_\psi \tag{15}$$

The third and final constraint for the iCST aero-line, C.8, is a second derivative constraint. The function coefficients and constant terms from Eq. (5) can therefore be written as:

$$a_{3,n} = [BP_{1,n} + BP_{2,n} \ldots + BP_{n-1,n}]''C(\psi) + 2([BP_{1,n} + BP_{2,n} \ldots + BP_{n-1,n}]'C(\psi)') + [BP_{1,n} + BP_{2,n} \ldots + BP_{n-1,n}]C''(\psi) \tag{16}$$

$$b_{3,0} = \xi''(\psi) - A_0 BP_{0,n} C''(\psi) - A_n BP_{n,n} C''\psi - 2[A_0 BP'_{0,n} C'(\psi) + A_n BP'_{n,n} C'\psi] - A_0 BP''_{0,n} C_\psi - A_n BP''_{n,n} C_\psi \tag{17}$$

The HiCST curve is constructed from a forebody curve (HiCST$_A$) and an afterbody curve (HiCST$_B$). These HiCST$_A$ and HiCST$_B$ curves (Table 1) can be calculated in the same way as the iCST curve with the only differences being their order (3rd and 6th respectively) and that the HiCST$_B$ curve has a third derivative constraint. G^2 geometric continuity is ensured by setting $C.6$ and $C.7$ equal to the first and second derivatives of HiCST$_A$ evaluated at the intersection point. Further G^n geometric continuity could be ensured in a similar manner by the imposition of derivatives up to the nth order. For a 6th order CST the matrix of coefficient becomes:

$$\mathbf{A} = \begin{bmatrix} a_{1,1} & a_{1,2} & \dots & a_{1,5} \\ a_{2,1} & a_{2,2} & \dots & a_{2,5} \\ \vdots & \vdots & \vdots & \vdots \\ a_{5,1} & a_{5,2} & \dots & a_{5,5} \end{bmatrix} \tag{18}$$

B is the matrix of constants which is defined as:

$$\mathbf{B} = \begin{bmatrix} b_{1,0} & b_{2,0} \dots & b_{5,0} \end{bmatrix}^T \tag{19}$$

X is the matrix of Bernstein Polynomial coefficients:

$$\mathbf{X} = \begin{bmatrix} bp_1 & bp_2 \dots & bp_5 \end{bmatrix}^T \tag{20}$$

Finally the CST function coefficients and constants for a third derivative constraint are given by Equations (21) and (22)

$$\begin{aligned} a_{i,n} = {} & [BP_{1,n} + BP_{2,n} \dots + BP_{n-1,n}]'''C(\psi) \\ & + 3([BP_{1,n} + BP_{2,n} \dots + BP_{n-1,n}]'C(\psi)'' \\ & + [BP_{1,n} + BP_{2,n} \dots + BP_{n-1,n}]''C(\psi)') \\ & + [BP_{1,n} + BP_{2,n} \dots + BP_{n-1,n}]C'''(\psi) \end{aligned} \tag{21}$$

$$\begin{aligned} b_{i,0} = {} & \xi''(\psi) - A_0 BP_{0,n} C'''(\psi) - A_n BP_{n,n} C'''\psi \\ & - 3[A_0 BP'_{0,n} C''(\psi) + A_0 BP''_{0,n} C'(\psi) \\ & + A_n BP'_{n,n} C''\psi + A_n BP''_{n,n} C'\psi] \\ & - A_0 BP'''_{0,n} C_\psi - A_n BP'''_{n,n} C_\psi \end{aligned} \tag{22}$$

3. Case study 1: fan cowl aerodynamics

3.1. Problem statement

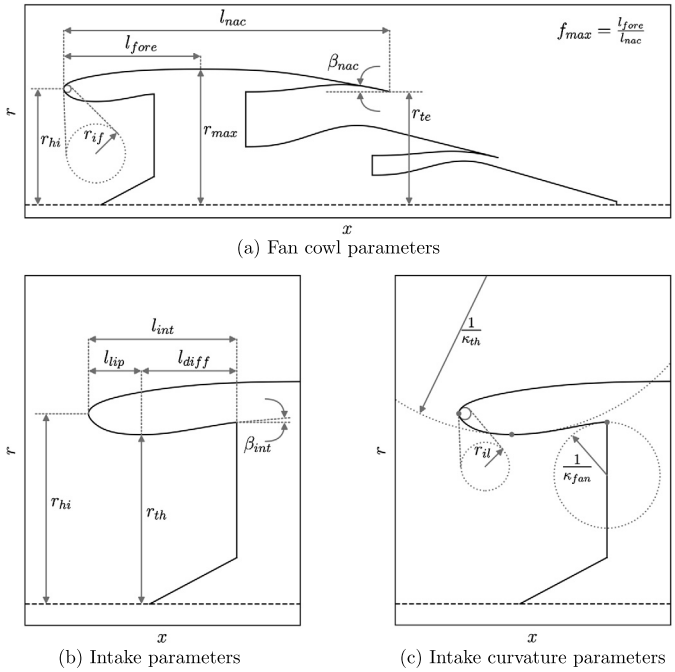
There is a need to develop more compact fan-cowls for aero-engines to reduce drag and weight [31]. These designs are inherently more challenging having been demonstrated to potentially result in very high wave drag [32,33,30] and an approach is required to explore and define the viable design space. The method should be capable of producing realistic shapes with smooth curves, reproduce a wide variety of different designs with a small number of input variables, be intuitive and be homogeneous in the design space [31]. This makes fan cowl design an ideal configuration to test and demonstrate the potential benefits of the HiCST parameterisation allowing more design fidelity without an increase in the dimensionality of the parameterisation.

Firstly, a design space exploration with Latin Hypercube Sampling was performed which consisted of 400 geometries. Secondly, a multi-objective optimisation was carried out to assess the impact on Pareto-optimal geometries due to changes in the geometrical parameterisation. Finally, the detailed aerodynamics of two fan cowl designs are discussed to explain the underlying cause of the improvement in integral aerodynamic parameters.

One significant challenge of nacelle design is the broad range of operating conditions at which they need to perform adequately [31]. Therefore, the present analysis was conducted for different flight conditions that are met during the aircraft mission. The flight conditions were set to reflect the operating conditions for future turbofan engines with $M_\infty = 0.85$, MFCR = 0.7; $M_\infty = 0.87$, MFCR = 0.7; $M_\infty = 0.85$, MFCR = 0.65 at h = 35kft to assess the mid-cruise drag, impact of increased Mach number and spillage drag relative to mid-cruise drag, respectively.

3.1.1. Fan cowl aerodynamic performance assessment methodology

To determine the performance of the fan cowls from the CFD data, the modified near-field method [34] was used. The fan cowl drag (D_{nac}) [35] includes contributions from pre-entry (ϕ_{pre}) stream-tube force, skin friction and pressure which acts on the external fan cowl surface and post-exit forces (ϕ_{post}) (Eq. (23)). The modified near field method allows the pre-entry stream-tube force and fan cowl external forces to be computed concurrently so that the highlight stagnation point does not need to be determined. The post-exit bounding stream-tube was determined from the trailing edge of the fan cowl and the pressure forces integrated along it to calculate the post-exit axial force.



(a) Fan cowl parameters

(b) Intake parameters

(c) Intake curvature parameters

Fig. 3. Geometric parameterisation.

$$D_{nac} = \phi_{pre} + \phi_{nac} + \phi_{post} \tag{23}$$

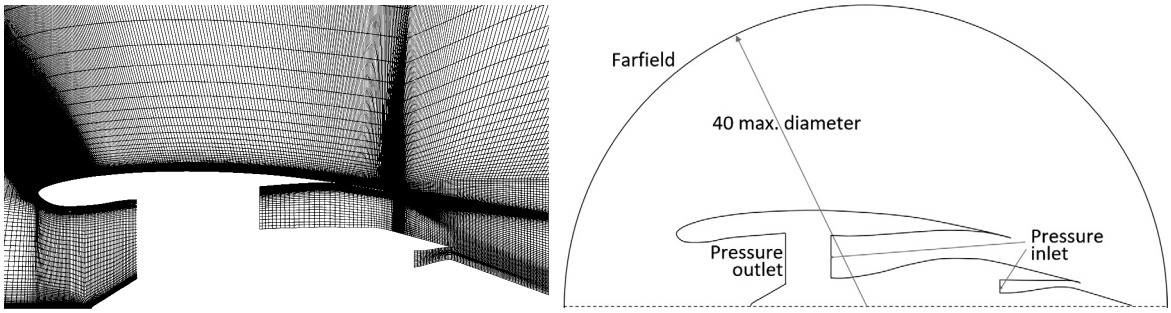
Three performance metrics are considered for the two fan cowl designs. The most important aerodynamic metric in fan cowl design is the drag incurred in cruise. This is represented as a coefficient of drag at mid-cruise ($c_{D,cruise}$) which for the considered engine cycle corresponds to $M_\infty = 0.85$, MFCR=0.7, $Re = 38 \times 10^6$. However, throughout cruise, the mass flow of the engine is typically reduced to account for the reduced mass of the aircraft and the lower incidence required as fuel is burnt. As a result, the MFCR is reduced and there is an associated spillage drag [36]. The impact of this spillage is sufficiently important such that the range of MFCRs throughout cruise should be considered. In this work the spillage drag ($c_{D,spill}$) is defined as the change in drag between the cruise condition ($M = 0.85$, $MFCR = 0.7$) and an end of cruise condition ($M = 0.85$, $MFCR = 0.65$).

Another key metric for nacelle aerodynamic performance is the sensitivity of the nacelle drag to increases in flight Mach number [36,31]. For large computational datasets such as those investigated in §3.5.1 and §3.5.2, sensitivity to increased flight Mach number can be assessed with Equation (24) [31].

$$\Delta C_{D-Mach} = \frac{D_{nac,M=M_\infty+0.02} - D_{nac,M=M_\infty}}{\frac{1}{2}\rho_\infty V_\infty^2 A_{hi}} \tag{24}$$

3.2. Geometric parameterisation

A design space exploration and optimisation was carried out on five nacelle geometric parameters, r_{if}, r_{max}, f_{max}, β_{nac}, r_{TE} (Fig. 3a) for a fixed highlight (l_{int}, r_{hi}) and trailing edge position



(a) 2D axisymmetric mesh for fan cowl studies (b) 2D axisymmetric domain for fan cowl studies

Fig. 4. Computational meshes and domains for the 2D fan cowl CFD calculations.

Table 2
Sample fan cowl parameterisation (Fig. 3a).

#	Parameter
$P.1_{fc}$	r_{hi}
$P.2_{fc}$	r_{te}/r_{hi}
$P.3_{fc}$	l_{nac}/r_{hi}
$P.4_{fc}$	r_{if}/r_{hi}
$P.5_{fc}$	r_{max}/r_{hi}
$P.6_{fc}$	f_{max}
$P.7_{fc}$	β_{nac}

Table 3
Constraints for Fan Cowls A and B.

#	Fan Cowl: Type	ψ	A $\xi^{(k)}(\psi)$	B (Forebody) $\xi^{(k)}(\psi)$	B (Afterbody) $\xi^{(k)}(\psi)$
$C.1_{fc}$	Position	0.000	0.263	0.263	0.263
$C.2_{fc}$	Position	1.000	0.240	0.240	0.240
$C.3_{fc}$	R	0.000	5.7×10^{-3}	5.7×10^{-3}	5.7×10^{-3}
$C.4_{fc}$	Position	0.307	1.172	1.172	1.172
$C.5_{fc}$	Gradient	0.307	0.000	0.000	0.000
$C.6_{fc}$	2nd derivative	0.307	n/a	n/a	$\frac{d^2y}{dx^2}\Big\|_{B_{forebody}}$
$C.7_{fc}$	3rd derivative	0.307	n/a	n/a	$\frac{d^3y}{dx^3}\Big\|_{B_{forebody}}$
$C.8_{fc}$	2nd derivative	1.000	-4.431	n/a	-4.431
$C.9_{fc}$	Gradient	1.000	0.217	0.217	0.217

$(l_{nac} - l_{int}, r_{te})$. Additionally an iCST designed fan cowl (Fan Cowl A) and its corresponding HiCST design (Fan Cowl B) have been selected from the DSE to illustrate both how the geometric parameterisation was applied and the potential aerodynamic improvement in cruise (§3.5.3).

The selected fan cowls had a fineness ratio $(2r_{max}/L_{nac})$ of 1.62 (Fig. 3a). The highlight, $(r_{hi}$, Fig. 3a), trailing edge radius, $(r_{te}$, Fig. 3a), and maximum radius, $(r_{max}$, Fig. 3a), were representative of a slim fan cowl design. The axial location of the maximum diameter was defined by an f_{max}, (L_{fore}/L_{nac}) of 0.307. Finally a boat-tail angle (β_{nac}) of approximately 12^o was used (Table 2 and Fig. 3a).

The fan cowl parameters can be turned into iCST constraints by non-dimensionalising with l_{nac} (Fig. 3a). For Fan cowl A, which used the iCST parametrisation, this resulted in 7 constraints. Two of these constraints ($C.1_{fc}$ and $C.2_{fc}$, Table 3) dimensionalise the curve and set the endpoints. The remaining 5 constraints ($C.3_{fc}$ to $C.5_{fc}$, $C.8_{fc}$, $C.9_{fc}$, Table 3) result in a 4th order iCST curve. The HiCST parameterisation of Fan Cowl B is more complicated, comprising two iCST curves which intersected in x, y, y', y'' and y''' at the maximum radial position (Fig. 2). The fan-cowl fore-body and after-body are formed by parts of two separate iCST curves (Fig. 2).

To improve the curvature distribution over the fore-cowl the order of the fore-body HiCST curve was reduced by removing constraint $C.8_{fc}$ (Table 3). This 2nd derivative constraint along with the co-located gradient constraint $(C.9_{fc})$ set the trailing edge radius of curvature (Eq. (25)). This means that the fore-body HiCST has an order of 3. To ensure curvature (G^2) and rate of change of curvature (G^3) continuity [37] at the maximum diameter two additional constraints were imposed on the after-body HiCST ($C.6_{fc}$ and $C.7_{fc}$). The magnitude of these constraints was set equal to that of the fore-body HiCST. In this way, though the order of the curve is increased (from 4 to 6), the overall degrees of freedom between Fan Cowl A and B remain unchanged.

$$\kappa = \frac{\frac{\partial^2 y}{\partial x^2}}{\left[1 + \left(\frac{\partial y}{\partial x}\right)^2\right]^{\frac{3}{2}}} \tag{25}$$

The HiCST fan cowl, Fan Cowl B, consisted of a fore-body and an after-body which had different parameterisations. The constraints applied to the curves are summarised in Table 3. The iCST parameterisation has 7 design parameters (Table 2) which are translated into 7 constraints (Table 3) on a fourth order iCST curve. Although the HiCST curve is constructed from two iCST curves of order 3 and 6 respectively it has the same number of degrees of freedom as the iCST parameterisation. This is because the same 7 design parameters (Table 2) are used for both and the additional constraints applied to the HiCST after-body curve (Table 3) are fully defined by constraints $C.1_{fc}$ to $C.5_{fc}$ and $C.9_{fc}$. This is an important aspect of the HiCST approach in this instance as the retention of the number of degrees of freedom means that the HiCST parameterisation can be employed without additional complexity. In this respect, any improvement gained from the hybrid approach effectively adds no computational expense. Once the constraints have been established, the Bernstein Polynomial coefficients can be calculated using the iCST methodology. The resultant curves (Fig. 2) demonstrated that greater control of the curvature distribution could be obtained through the use of a HiCST.

3.3. Analysis

All CFD calculations were carried out with an implicit, Favre-averaged Navier-Stokes, density based approach. The two-equation SST $k - \omega$ turbulence model [38] was solved. The working fluid, air, was modelled as an ideal compressible gas with viscosity calculated using Sutherland's Law. The convective fluxes were discretised by the Roe-FDS method. Solution convergence was monitored using both the scaled residuals and the forces on all walls. Solutions were deemed to be converged when these terms were below 1×10^{-5} and iteration-independent respectively.

The fan cowl definition is two-dimensional and an axisymmetric CFD model was used to reduce computational cost (Figs. 4a & 4b). A domain independence study was carried out for a fan cowl

with three domain sizes. The semi-circular domains had radii of $40r_{max}$, $60r_{max}$ and $80r_{max}$ where r_{max} is the maximum nacelle radius (Fig. 4b). The change in cruise nacelle drag predicted from the simulations with the largest two domains was 0.1% and so the largest domain was chosen for all further computations.

A multi-block structured mesh was produced for the fan cowl geometries of approximately 70000 cells. A mesh independence study was carried out with three grids of 35000, 70000 and 140000. In accordance with the method proposed by Roache [39] it was found that the 70000 cell grid led to spatial discretisation errors less than 1% in nacelle drag. Previous work has shown that the CFD method and process used in this study is useful for the analysis of nacelle aerodynamics and validation studies show that the method provides a maximum uncertainty of up to 4% on pre-drag-rise nacelle drag, a difference of ± 0.003 on M_{DR} (Equation (24)) and typically a prediction of critical MFCR within 2% of the measured data [36,40].

3.4. Design space exploration and optimisation setup

Initially, a design space exploration was carried out which consisted of 400 iCST and HiCST designs to compare the nacelle drag characteristics with the different parametrisations. Subsequently, a multi-objective optimisation with each method was performed to identify a set of Pareto optimal solutions. The analysis is based on the framework developed by Tejero et al. [31,41] for the aerodynamic nacelle design of future turbofan engines. The tool encompasses different modelling methods that include geometry definition using Class Shape Transformations, aerodynamic simulation and analysis, evaluation at various operating conditions and a genetic algorithm. The Non-dominated Sorting Genetic Algorithm II (NSGA-II) [42] is employed due to its global optimisation characteristics in transonic flow aerodynamic applications [30]. The optimisation routine is started with a Latin Hypercube Sampling (LHS) design space exploration of 400 samples and subsequent generations are formed by 50 individuals. This selection is based on a statistical analysis that demonstrated the improved convergence to the Pareto front for aerodynamic nacelle design applications [30]. Overall, a total number of 30 generations were required to ensure a variation on the hypervolume below 1% on the last three generations. As such, more than 5000 CFD simulations were performed throughout each optimisation routine.

3.5. Results and discussion

3.5.1. Design space exploration

The iCST method has been demonstrated to be useful for the construction of nacelle aero-lines [43]. An assessment of the iCST designs indicates that there are some limitations associated with inflections in the radius on the fore-body of the cowl. An inflection occurs when the curvature changes polarity and generally results in detrimental aerodynamics. In this study, for the 400 iCST designs, 71 had inflections on the fore-body. As expected, these 71 cases had a notably higher mean cruise drag of $C_{D,cruise} = 0.0467$ compared to the mean value of $C_{D,cruise} = 0.0366$ for the designs without a geometric inflection. Of the 71 designs which had an inflection in the iCST formulation, only 3 had inflections on the fore-body when created with HiCSTs. For those 71 designs, 20 had all three metrics improved relative to the iCST version, whilst none had all three metrics worsened (Fig. 5). In addition, the average cruise drag of these 71 designs in the HiCST formulation dropped to 0.0383 (a decrease of 18%. Fig. 5). An example of this subset is provided in Fig. 6a which illustrates the presence of an inflection in the curvature distribution for the iCST design and the absence of this inflection for the HiCST design. In this case the improvement from a HiCST was a reduction in cruise drag from $C_{D,cruise} = 0.0329$ to $C_{D,cruise} = 0.0286$, in spillage drag from $C_{D,spill} = 0.0138$ to $C_{D,spill} = 0.0113$ and $C_{D,Mach} = 0.7322$ to $C_{D,Mach} = 0.0083$ in $C_{D,Mach}$. This considerable improvement in the response to Mach number indicates that the use of HiCST to remove inflections from the designs allows a much improved design space and enables designs which would be poorly performing with an iCST formulation.

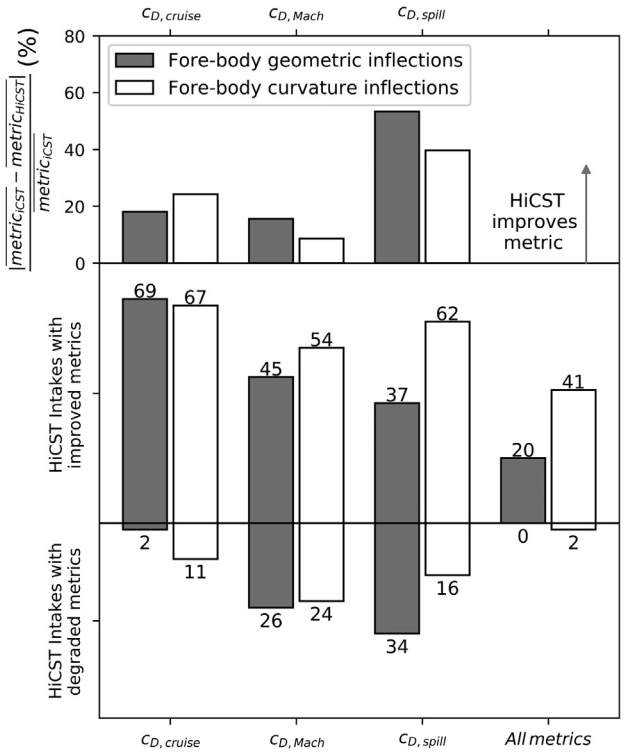


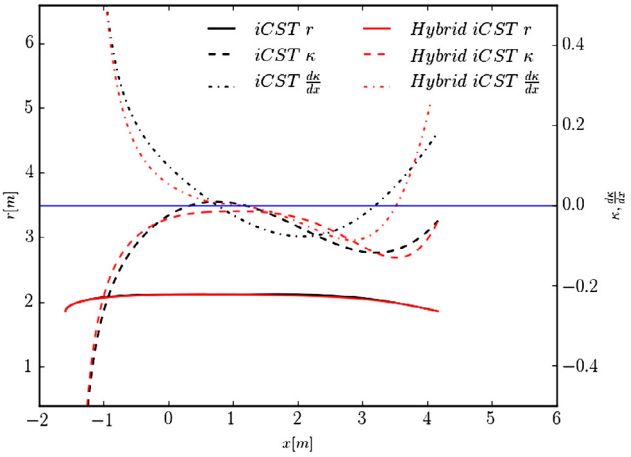
Fig. 5. A comparison between the aerodynamic performance of the HiCST and iCST parameterisations applied to an aero-engine fan cowl. The aerodynamic performance benefit is illustrated for two subsets of the iCST design space in which there were geometric and curvature inflections respectively.

Another subset of the 400 fan cowl designs which have on average poor aerodynamics for the iCST formulation are those with inflections in the curvature on the fore-body of the nacelle. There were 78 cases, (Fig. 5), with this type of inflection in the iCST design space whereas there were only 2 in the HiCST design space. Of the 78 designs from the iCST design space in the HiCST design space 41 were improved in all three aerodynamic metrics, whilst two were worsened in all metrics (Fig. 5). On average, the cruise drag for these 78 designs was reduced from 0.0479 in the iCST formulation to 0.0363 with the HiCSTs (a decrease of 24%, Fig. 5). An example from this subset (Fig. 6b) demonstrates the removal of the curvature inflection which occurs on the fore-body of the iCST design. In this singular case the improvement from a HiCST was a reduction in cruise drag from $C_{D,cruise} = 0.0282$ to $C_{D,cruise} = 0.0221$, in spillage drag from $C_{D,spill} = 0.0080$ to $C_{D,spill} = 0.0072$ and $C_{D,Mach} = 0.0084$ to $C_{D,Mach} = 0.0074$ in $C_{D,Mach}$.

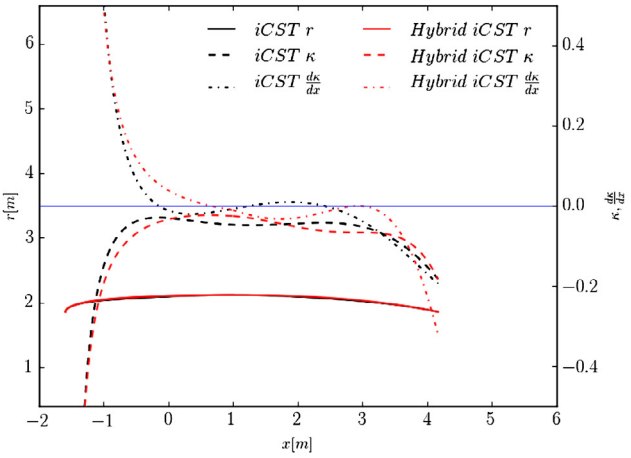
Overall this shows the potential aerodynamic performance benefit of employing the HiCST parameterisation as opposed to the iCST approach. These performance benefits are especially apparent in the challenging regions of the design space where it is not always possible to construct an iCST based curve without any inflections present in the geometry or curvature distributions.

3.5.2. Optimisation

Both the iCST and HiCST fan-cowl parametrisations methods have been applied to the multi-objective optimisation (MOO) of a civil aero-engine with L_{nac}/r_{hi} = 2.4 and r_{te}/r_{hi} = 1.0. This is a



(a) Example design with a forebody inflection in the radius



(b) Example design with a forebody inflection in the curvature

Fig. 6. Example fan cowl geometries from the design space exploration.

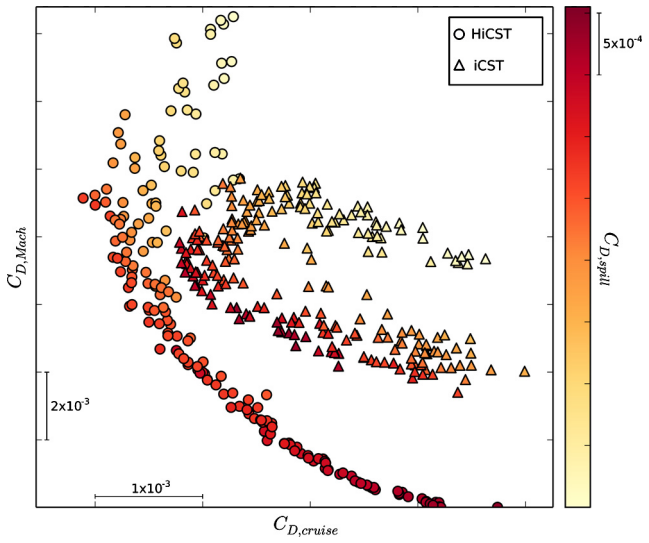


Fig. 7. Pareto front comparison between the HiCST and iCST parameterisations applied to an aero-engine fan cowl.

Table 4
Nacelle performance metrics for Fan Cowls A and B.

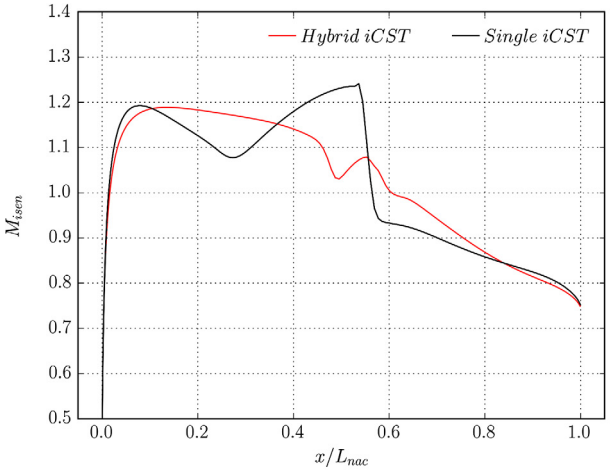
Fan cowl	A (iCST)	B (HiCST)
$c_{D,cruise}$:	0.0300	0.0227
M_{DR}:	0.822	0.850

compact configuration within the expected design space for future turbo-fan engines, in which previous investigations have underlined the associated non-linear characteristics of the nacelle transonic flow aerodynamics [31]. As such, it is a complex design to test the proposed HiCST parametrisation approach.

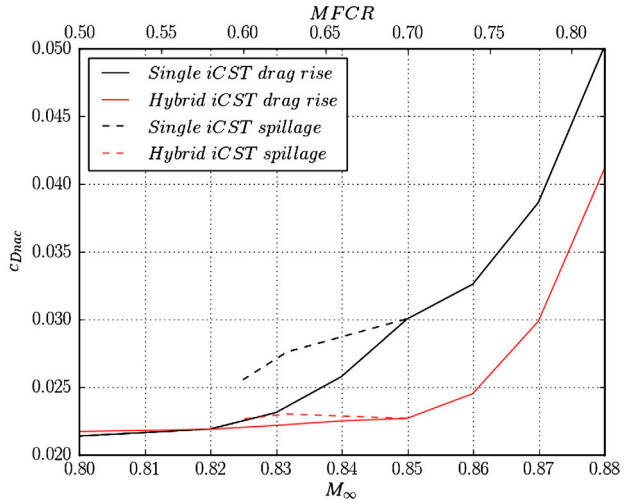
Two independent multi-objective optimisation routines were carried out with the aforementioned established method of 30 generations with an initial design space exploration of 400 nacelle designs and subsequent generations of 50 individuals. The optimisation process resulted in a three-dimensional set of Pareto optimal solutions. Fig. 7 presents the projection of the Pareto front on the $C_{D,cruise} - C_{D,Mach}$ space and coloured by $C_{D,spill}$. The representation clearly highlights the benefits of the proposed HiCST formulation over the traditional iCST method. Relative to the iCST approach, the minimum achievable nacelle cruise drag was reduced by 3.9% with the HiCST parametrisation. Besides, this method also presents benefits in terms of a lower sensitivity to the change of flight Mach number. While there are designs with $C_{D,Mach} \approx 0$ and a concomitant $C_{D,cruise}$ = 0.0252, the iCST method leads to a minimum $C_{D,Mach}$ = 0.0034 at similar value of nacelle cruise drag ($C_{D,cruise}$). On the other hand, both parametrisations present nacelle designs which are insensitive to changes on massflow capture ratio ($C_{D,spill} \approx 0$) at the expense of large $C_{D,cruise}$ and $C_{D,Mach}$ (Fig. 7).

3.5.3. Fan cowl performance at cruise

The HiCST parametrisation can provide an aerodynamic benefit over the iCST approach. This potential performance benefit is particularly apparent in the challenging regions of the fan cowl design space where geometric inflections or inflections in the curvature distribution cannot be avoided with a single iCST curve. To illustrate this two fan cowl configurations were simulated for a range of aerodynamic conditions to assess the cruise drag, the impact of reduced MFCR and sensitivity to increased Mach number. These two configurations had the same geometric parameters (Table 2) and only differed in that Fan Cowl A was created with an iCST approach and Fan Cowl B was created with HiCST curves. The range of mass flows was intended to capture a cruise phase at constant $M_\infty = 0.85$. Fan cowl B, with a HiCST curve, demonstrated that a lower cruise drag and a beneficial higher drag rise Mach number could be achieved (Table 4) relative to the single iCST fan cowl. Cruise drag, at $M_\infty = 0.85$, $MFCR = 0.7$, was reduced by 24% whilst the drag rise Mach number was increased by $\Delta M_{DR} = 0.028$. This represents a considerable delay in the transonic penalty by simply using a HiCST. The reason for the improved performance is solely from the de-coupling of the fore-body and after-body since the intuitive parameters used to define the cowl were identical between Fan cowl A and B (Table 2). Across the forward region of the cowl ($x/L_{nac} < 0.1$), the gradient (dr/dx) changes less rapidly for the HiCST design relative to the iCST design as the hybrid fore-body is less constrained by the parametrization (Fig. 2). This results in a delay of the peak fore-body acceleration on Fan Cowl B relative to Fan Cowl A (Fig. 8a). In addition, the single iCST curve has greater values of the second derivative immediately after the maximum radius (Fig. 2) which results in a second acceleration for Fan Cowl A (Fig. 8a). This causes the Mach number to increase compared to the HiCST fan cowl (Fig. 8a) and an after-body shock occurs for Fan Cowl A as a result. Due to this strong after-body shock, the drag of Fan Cowl A is significantly worse than Fan Cowl B. The increased shock strength also causes the drag rise to occur at lower Mach number (Fig. 8b) since the onset of drag rise is caused by excessive wave drag. This results in an increase of $\Delta M_{DR} = 0.028$ for Fan Cowl B relative to Fan Cowl A (Table 4). In addition, the drag is found to



(a) Isentropic Mach number distribution for the two fan cowl configurations in cruise $M_\infty = 0.85$, $Re = 38 \times 10^6$



(b) Fan cowl drag as a function of freestream Mach number at constant MFCR=0.7 (solid) and as a function of MFCR at constant freestream Mach number M=0.85 (dashed)

Fig. 8. The aerodynamic performance of an iCST and equivalent HiCST fan cowl in a challenging region of the design space.

be consistently higher for Fan Cowl A, with the single iCST, for all MFCRs expected throughout the cruise phase of the flight (Fig. 8b) which would result in an overall higher fuel burn if this fan cowl were integrated with an engine.

4. Case study 2: intake aerodynamics

4.1. Problem statement

As aero-engine specific thrust decreases to improve fuel burn and to reduce noise and emissions, the fan diameter can increase [44]. Innovative intake and nacelle designs are required to reduce the associated increases in weight and drag [34]. One such approach is a reduction in intake length [45]. The short intake design approach however can result in increased flow non-uniformity at the fan face as well as a reduction in the ability of the intake to efficiently diffuse the flow from the throat to the fan face. The intake design challenge is then to design short intakes without comprising intake and fan performance.

The iCST parameterisation can be used to generate aero-engine intake geometries [28]. However in some parts of the design space the iCST approach is limited by its inherent mathematical smoothness. This restricts the viable design space. This limitation is particularly apparent in short intake design where the lip and the diffuser are closely coupled. This can potentially be overcome through the use of the HiCST parameterisation.

Within this context two intakes have been designed to compare the iCST and Hybrid iCST approaches (Intakes A and B respectively) for a challenging high incidence condition using the methods outlined in §4.1.1. This aerodynamic configuration is representative of the off-design $C_{L,max}$ condition which is the largest angle of attack which the engine is typically expected to be subjected to in flight [45].

4.1.1. Intake performance assessment methodology

The aerodynamic performance of the intake configurations are assessed with four metrics. Intake Pressure Recovery (IPR) is a measure of total pressure losses in the duct given by,

$$IPR = \frac{\overline{P}_{0,fan\ face}}{P_{0,\infty}} \tag{26}$$

where $\overline{P}_{0,fan\ face}$ is the area-averaged total pressure on the fan face and $P_{0\infty}$ is the freestream total pressure.

Total pressure distortion in the fan face plane is assessed with DC_{60} [46,47] defined as,

$$DC_{60} = \frac{\overline{P}_{0,fan\ face} - P_{60}}{q} \tag{27}$$

where P_{60} is the mean total pressure in the 60^o sector with the lowest mean total pressure and q is the dynamic pressure. This total pressure distortion parameter, (DC_{60}), can provide an indication to the presence of flow separation within the intake. [48] The typical upper limit on DC_{60} for a civil subsonic aircraft is 0.2. [49] The presence, extent and initial cause of flow separation is assessed for each intake design. The final aerodynamic metric studied is the peak isentropic Mach number,

$$M_{isen} = \sqrt{\frac{2\left[\left(\frac{P_{0,\infty}}{P}\right)^{\frac{\gamma}{\gamma-1}} - 1\right]}{\gamma - 1}} \tag{28}$$

where $P_{0\infty}$ is the freestream total pressure, P is the local static pressure and γ is the ratio of specific heats. The peak isentropic Mach number is a measure of the flow acceleration around the intake lip. Flow acceleration can lead to the formation of a shock, in this case the maximum isentropic Mach number can be an indicator of shock strength.

4.2. Geometric parameterisation

The NASA Common Research Model CRM [50] is representative of a twin-engined, wide-body, civil, transport aircraft. The CRM has a cruise design point of M=0.85 at a wing chord Reynolds number of 40×10^6. Two intakes were designed for this operating point. The intake was sized for a mass-flow capture ratio of 0.75, fan hub to tip ratio of 0.3 [51] and a fan face Mach number of 0.6 [51]. Based on conventional intake design rules the average throat Mach number should be less than 0.75 [52] and for this study a value of 0.72 was used to size the throat. The non-dimensional intake ($L_{int}/(2r_{fan})$) was set to 0.35 (Table 5 and Fig. 3) and is representative of a future short intake design [28].

Intake A was constructed with a single iCST curve which employed the round nosed airfoil Class Function ($C^{1.0}_{0.5}$). Parameters $P.1_{int}$ to $P.3_{int}$ set the endpoints of the intake aero-line (Fig. 9). The radius of curvature at the highlight, (r_{il}), was set by $P.4_{int}$ us-

Table 5
Parameterisation of Intakes A (iCST) and B (HiCST) (Fig. 3c).

	Intake:	A	B	
#	iCST	Single	HiCST lip	HiCST diffuser
$P.1_{int}$	r_{hi}	-	-	-
$P.2_{int}$	r_{fan}/r_{hi}	0.964	y^*m	0.964
$P.3_{int}$	l_{int}/r_{hi}	0.675	0.675	0.675
$P.4_{int}$	f_{il}	0.700	0.700	0.700
$P.5_{int}$	CR	1.263	1.263	1.263
$P.6_{int}$	AR	2.5	2.8	2.8
$P.7_{int}$	$\kappa_{th} r_{hi}$	1.601	1.299	1.299
$P.8_{int}$	β_{int}	0^o	$\tan^{-1}(dy/dx)^\dagger$	3^o
$P.9_{int}$	$\kappa_{fan} r_{hi}$	2.135	0.000	2.135

* denotes that the parameter was set to maximise the smoothness of the curve between the highlight and the throat.

† indicates that the parameter was set such that d^2r/dx^2 at $\psi = 1$ was equal to zero.

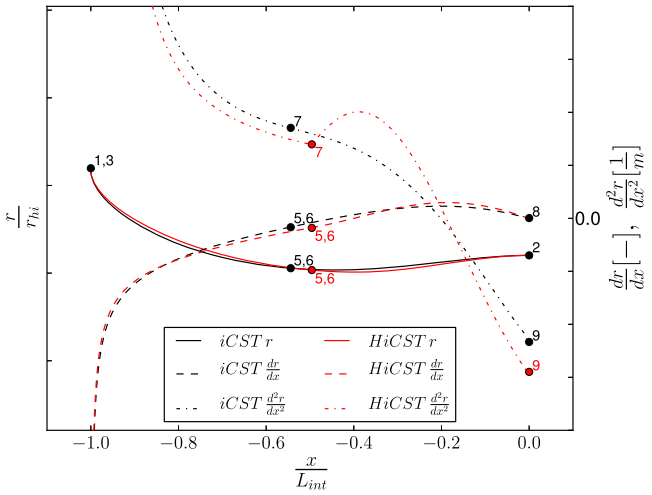


Fig. 9. Geometry, first and second order spatial derivatives of r w.r.t. to x and the imposed constraints for Intake A (iCST) and Intake B (HiCST).

ing Equation (29).

$$r_{il} = f_{il}\frac{(r_{hi} - r_{th})^2}{l_{lip}} \tag{29}$$

Through a design iteration process, the gradient and curvature at the juncture between the intake and the fan face reference plane was set to 0^o and $-1.2m^{-1}$ respectively ($P.8_{int}$ and $P.9_{int}$, Table 5). Intake design guidelines state that the maximum diffuser angle (Eq. (30)) should not exceed 7^o to avoid diffusion driven separation within the intake [53].

$$\theta_{max,diff} = \max\left(\tan\frac{dr}{dx}\right)\Big|_{x_{th}}^{x_{fan}} \tag{30}$$

$\theta_{max,diff}$ is a function of the throat location and the curvature at this point (κ_{th}). These parameters also influence the curvature distribution over the intake lip. The location of the throat (Fig. 3c) is set through the intake contraction ratio (CR, Eq. (31)) and lip aspect ratio (AR, Eq. (32)).

$$CR = \frac{A_{hi}}{A_{th}} = \left(\frac{r_{hi}}{r_{th}}\right)^2 \tag{31}$$

$$AR = \frac{l_{lip}}{r_{hi} - r_{th}} \tag{32}$$

CR, AR and κ_{th} were set by an iterative design process which sought to maximise the smoothness of the lip curvature distribution by minimising $f_{\kappa''}(x)$ (Eq. (33)) while not exceeding $\theta_{max,diff} = 7^o$.

$$f_{\kappa''}(x) = \frac{d^2R}{dx^2} \text{ where } R = \frac{1}{\kappa} \tag{33}$$

The resultant design had CR, AR and κ_{th} of 1.263, 2.5 and 0.9 m^{-1} respectively (Table 5). Intake A was a compromise between diffuser angle and lip smoothness due to the characteristic mathematical smoothness of an iCST curve. As a result of this compromise the lip curvature distribution was non-monotonic (Fig. 9).

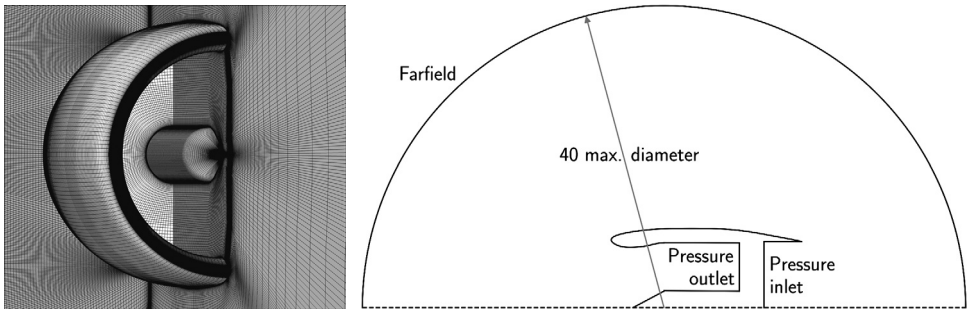
Intake B was designed to remove the curvature inflection present in the lip of Intake A. This necessitated the use of the HiCST approach to decouple the lip and diffuser designs. Intake B was constructed with the HiCST parameterisation. This consisted of two aero-lines namely the HiCST lip and the HiCST diffuser with intersected at the intake throat (Fig. 9). This approach was employed to allow the diffuser design to be altered independently of the lip design and vice versa. This would not have been possible with the iCST parameterisation. The HiCST diffuser was constructed using the same parameterisation as Intake A. However, the diffuser aero-line constraints could be set to maximise the aerodynamic performance of the diffuser without a trade-off in lip aerodynamic performance. The intake aero-line gradient at the juncture with the nominal fan face plane (β_{int}, Fig. 3b) was increased from 0^o to 3^o (Table 5) which decreased the maximum diffuser angle ($\theta_{max,diff}$, Eq. (30)). The throat curvature (κ_{th}) was also reduced from 0.9 to 0.73 to further reduce the maximum diffuser angle. This allowed the lip aspect ratio (AR, Eq. (32)) to be increased from 2.5 to 2.8 without exceeding a maximum diffuser angle of 7^o. An increase in AR at a fixed lip contraction ratio (CR, Eq. (31)) resulted in a longer intake lip (l_{lip}, Fig. 3b). $P.2_{int}$ was varied to achieve a smooth monotonic distribution of curvature from the highlight to the throat while $P.8_{int}$ was set so that d^2r/dx^2 at $\psi = 1$ was equal to zero. As AR increased from Intake A to Intake B while CR and F_{il} remained constant, r_{il}, the initial lip radius of curvature decreased. This, in conjunction with the decrease in throat curvature, led to a slight increase in the overall lip gradient of curvature ($(\kappa_{th} - \kappa_{il})/L_{lip}$) from $35.4m^{-2}$ to $35.9m^{-2}$. This meant that flow turning was more weighted towards the highlight than the lip. The gradient, and curvature, (κ_{th}), were imposed at the throat point to ensure curvature continuity (G^3) from the highlight. As the third derivative is not imposed at the throat the intake aero-line has a rate of change of curvature (G^4) discontinuity at this point (Fig. 9).

Overall these design changes, which were possible because of the HiCST parameterisation and the associated decoupling of the lip and diffuser constructions, resulted in a smooth monotonic distribution of curvature from the highlight to the throat and a reduction in maximum diffuser angle for Intake B in comparison to Intake A.

4.3. Analysis

The nature of the intake calculations necessitated a 3D CFD approach. The CFD method was otherwise identical to that described in §3.3. Meshes were constructed with a fully structured, multi-block approach [54] (Fig. 10a). The boundary layer was fully resolved such that the y^+ was approximately equal to 1 by the creation of a boundary layer block around all solid surfaces. This boundary layer block contained 50 cells with a maximum cell height expansion ratio of 1.2 To ensure a high quality mesh minimum values of equi-angle skewness and 2x2x2 determinant of 0.3 and 0.45 respectively were maintained.

A mesh independence investigation was carried out in line with standard practice [55]. The Grid Convergence Index (GCI) was calculated for three different levels of mesh refinement with 2.4, 4.8



(a) 3D mesh for intake studies (b) 3D domain for intake studies

Fig. 10. Computational meshes and domains for the 3D intake CFD calculations.

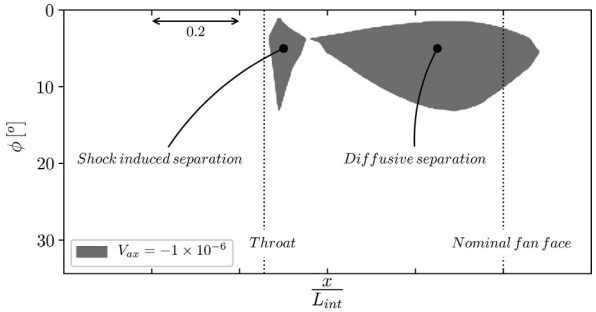
and 9.6 million cells each. Nacelle drag was used as the grid convergence metric with a GCI of 0.73% and 0.05% calculated for the coarsest and finest meshes respectively. This indicated that the 4.8 million element mesh was within a band of error with regards to nacelle drag between 0.05% and 0.73%. This level of mesh independence was deemed satisfactory and the mesh selected for all the high incidence intake calculations carried out for this paper. CFD predicted distributions of isentropic Mach number over the surface of an aero-engine intake have been compared to measured data at conditions representative of a climb-out. Peak isentropic Mach numbers were predicted within $\Delta M = 0.05$.

The overall size of the computational domain was defined as a function of the nacelle maximum diameter using a linear scaling factor of 40. The freestream conditions at infinity were modelled using a pressure far-field boundary condition (Fig. 10b). At this boundary the static pressure, static temperature, Mach number, velocity direction components and turbulence levels were specified. The engine massflow rate was controlled by a static pressure outlet boundary condition with a target massflow(Fig. 10b). At the pressure inlet boundary (Fig. 10b) total temperature and total pressure were set equal to freestream conditions [28].

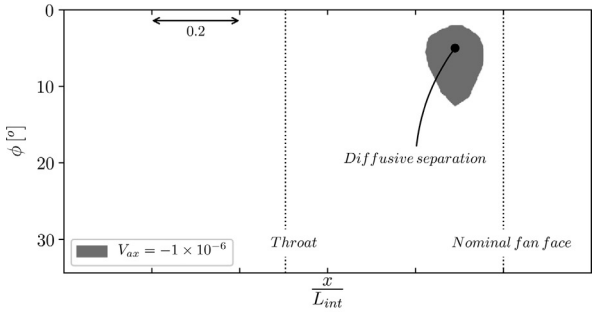
4.4. Results and discussion

For Intake A, the intake constructed with the iCST approach, the intake pressure recovery and maximum isentropic Mach number were calculated to be 0.9980 and 1.245 respectively. The DC_{60} parameter, which gives a measure of total pressure distortion at the fan face reference plane was calculated to be 0.047. A value of DC_{60} below 0.2 can indicate an aerodynamically acceptable design [49]. However, Fig. 11a shows two small regions of reverse flow in the intake. There is an initial shock induced separation of the intake boundary layer which reattaches (Fig. 12a). The shock, which is the root cause of this separation, can be seen in the isentropic Mach number distribution over the lower lip (Fig. 12a). The smooth curvature distribution around the lip allows the flow to accelerate around the lip to Mach 1.245 before a shock-wave is formed. The second region of reverse flow, (Fig. 11a), is due to a diffusion induced separation and it extends through the nominal fan face. The reasonable aerodynamic performance of this intake bottom aero-line demonstrates the capability of the iCST intake parametrization method.

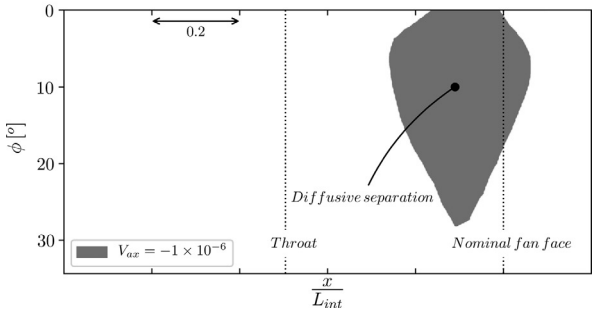
Intake B was constructed with the HiCST method. This approach allowed a smooth monotonic increase in the radius of curvature from the highlight to the throat to be specified (Fig. 9). The maximum isentropic Mach number was reduced from 1.245 to 1.241 relative to Intake A at the same conditions (Table 6). This improvement in the lip design removed the shock induced separation that was present for Intake A (Fig. 12a). The only separation present was a small diffusion induced separation which reattached before the fan face reference plane (Fig. 11b). Two aspects of Intake B's



(a) $M = 0.45$, $\alpha = 22^o$, $MFCR = 1.26$, Intake A



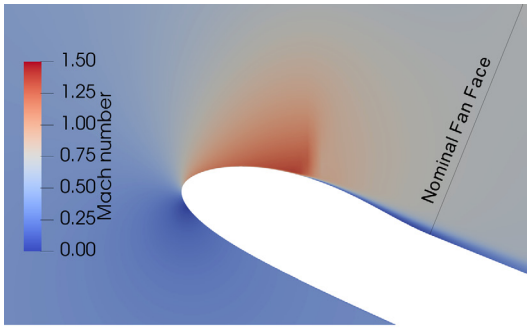
(b) $M = 0.45$, $\alpha = 22^o$, $MFCR = 1.26$, Intake B



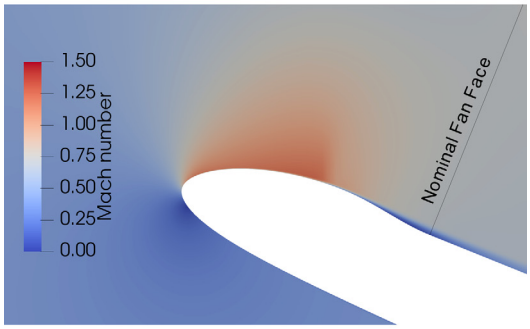
(c) $M = 0.45$, $\alpha = 26^o$, $MFCR = 1.26$, Intake B

Fig. 11. The extent of separated flow in the intake illustrated in cylindrical coordinates.

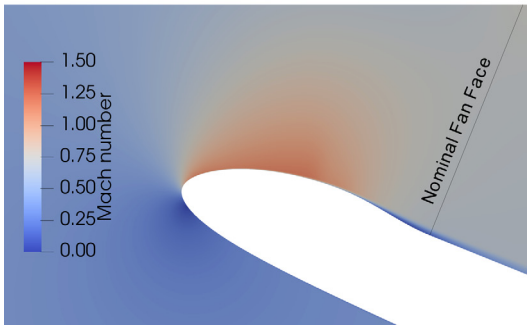
aerodynamic performance were noted as slight concerns: the shock position and isentropic Mach number distribution. The shock was located close to the throat (Fig. 12b) approximately co-located with an inflection in the curvature. This was consistent with previous intake designs [27] where it was noted that any shocks present are positioned approximately at points of inflection in the radius of curvature. Intake B was designed such that there were no inflection points in the radius of curvature of the lip, with the first inflection point located at the throat (Fig. 9). As an assessment of the robustness of the intake designs, sweeps of angle of attack and MFCR were carried out. These assessments were carried out both



(a) $M = 0.45$, $\alpha = 22^o$, $MFCR = 1.26$, Intake A.



(b) $M = 0.45$, $\alpha = 22^o$, $MFCR = 1.26$, Intake B.



(c) $M = 0.45$, $\alpha = 22^o$, $\Delta\dot{m} = -2\%$, Intake B.

Fig. 12. Mach number contours on the symmetry plane.

for Intake A and Intake B so that their aerodynamic performance could be compared across a range of conditions.

Table 6
Intake performance metrics.

Intake	A (iCST)	B (HiCST)
DC_{60}	0.047	0.025
IPR	0.9980	0.9984
$Max\,M_{isen}$	1.241	1.245

The intake aerodynamic performance was tested at increased angles of attack (Fig. 13). As expected both the isentropic Mach number and DC_{60} increased as the angle of attack was increased. Over the range of angle of attacks investigated ($22^o < \alpha < 26^o$) there were no step changes in performance, indicating that both intake designs are robust at the high incidence operating condition. Intake A has a higher total pressure distortion coefficient at 22^o angle of attack than Intake B and as angle of attack increased from 22^o to 26^o there was a much larger increase in DC_{60} from 0.047 to 0.182 as opposed to from 0.024 to 0.046 for Intake B. However, Intake A is less sensitive to angle of attack in terms of maximum isentropic Mach number than Intake B. For Intake A there is only a small increase in the maximum M_{isen} across the range of angle of attacks studied from 1.245 to 1.264. The reason that the maximum M_{isen} increases with incidence at a lower rate for Intake A in comparison to Intake B is the presence of a shock induced separation on the intake lip (Fig. 11a). This separation bubble forms a blockage and reduces the amount of flow turning around the lower lip which in turn leads to lower flow acceleration and lower maximum isentropic Mach numbers. It is for this reason that M_{isen} should not on its own be used as an intake performance metric but rather as an intake metric which can give an indication of the underlying flow physics. Across the range of angle of attacks investigated both shock and diffusive induced separations were present (Fig. 13). However, for Intake B only a diffusion induced separation was predicted. This area of diffusive separation increased in both the axial and circumferential direction as the angle of attack was increased and can clearly be seen at an angle of attack of 26^o (Fig. 11c). This area of separation now extends through the nominal fan face plane.

The sensitivity of both intakes aerodynamic performance to changes in massflow was assessed by increasing and decreasing massflow by 2% in increments of 1%. For Intake B at $\Delta\dot{m} = -2\%$ no intake separation was found, either shock induced or diffusion driven. The lack of a shock induced separation was expected as none was present for the baseline massflow case ($\Delta\dot{m} = 0\%$) and reducing the massflow rate reduces flow acceleration around the lip. The maximum isentropic Mach reduced was reduced to 1.176 from 1.245 in the baseline case. The presence of a weak shock is illustrated by contours of Mach number on the symmetry plane (Fig. 12c). This low isentropic Mach number and lack of separation results in a low DC_{60} of 0.018 and an intake pressure recovery of 0.9984. For Intake B when the intake massflow rate is increased by 2% from the baseline there is an increase in both DC_{60} and maximum isentropic Mach number occurs up to values of 0.053 and 1.314 respectively. At all massflow rates investigated below the baseline massflow rate ($\Delta\dot{m} = 0\%$) there is no flow separation present in Intake B. At $\Delta\dot{m} = 0\%$ a small diffusive separation is present (Fig. 11b) and when $\Delta\dot{m}$ is increased to 2% there is a diffusive and shock induced separation. Throughout all the massflow rates simulated no step changes in DC_{60} or maximum isentropic Mach number were found. This indicates that Intake B is a robust design for the intake high incidence operating condition. For all massflows investigated a diffusive and a shock driven separation were present in Intake A with little change in the flow physics across the range $-2\% \leq \Delta\dot{m} \leq 0\%$. Further increases in massflow rate to $\Delta\dot{m} = 1\%$ led to the separate shock and diffusive based separations merging which resulted in a step change increase in DC_{60} to 0.12. However this increase in DC_{60} is still below the acceptable DC_{60} limit of 0.2 [49].

The robust aerodynamic performance of Intake B and the improvement of its aerodynamic performance in comparison with Intake A illustrate the utility of the HiCST in intake design. As the HiCST approach does not necessitate an increase in the order of the curve the method is suited to preliminary and detailed design and optimisation of geometric definitions.

5. Conclusions

The iCST method has been applied to aero-engine fan-cowls and intakes. The mathematical smoothness inherent to curves constructed with the iCST approach has been shown to limit the design space for these geometries. A new parametrisation, HiCST, has been introduced. It is possible to implement this HiCST parametrization without an increase in the degrees of freedom used to define the geometry. This allows two sections of a single aero-line to be decoupled, without geometric discontinuity, whilst maintaining the dimensionality of a design problem.

A fan cowl design space exploration was carried out which employed the iCST parametrization. It was shown that in the

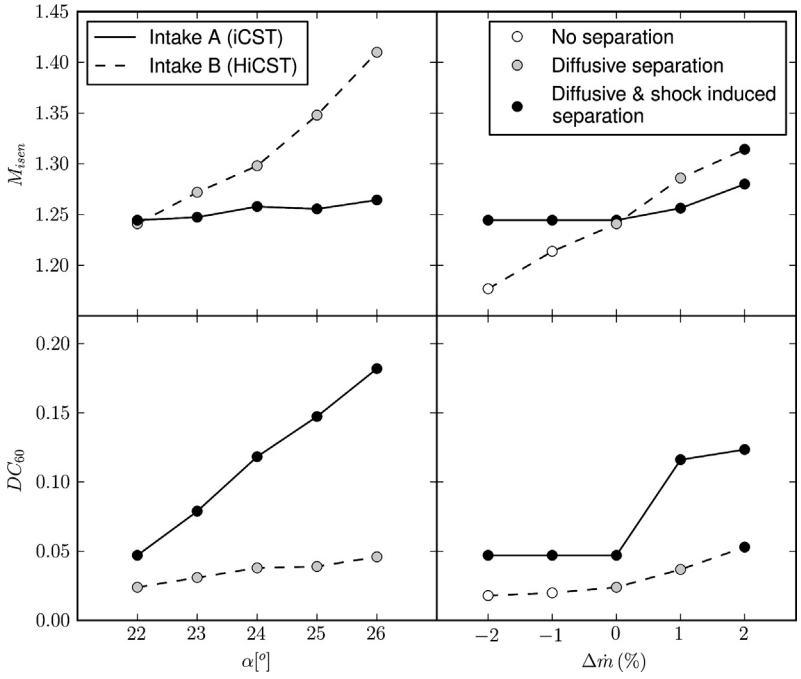


Fig. 13. Variation of maximum isentropic Mach number and DC_{60} with changes in angle of attack, $M = 0.45$, $MFCR = 1.26$.

large majority of cases when a radius inflection or a curvature inflection was present in the fan cowl fore-body the HiCST parametrization gave an aerodynamic performance benefit over the iCST parametrization. This aerodynamic benefit was achieved without an increase in the design degrees of freedom. In the example fan cowl design demonstrated within this paper, it was shown that this decoupling had resulted in a greatly improved design with a reduction in cruise drag of 24% relative to a standard iCST. The benefits of a decoupled HiCST curve can also be exploited to improve the drag rise performance of the fan cowl as a direct result of the reduced accelerations. Crucially, this improvement in the aerodynamics, without increased degrees of freedom, makes this implementation ideal for an optimisation problem where the aerodynamics of a fan cowl fore-body and after-body would otherwise be highly coupled.

The utility of the Hybrid iCST approach has also been shown through two intake design case studies. A single iCST intake, Intake A was designed to have a short intake with reasonable aerodynamic performance.

The use of the HiCST method in the design of Intake B allowed a discontinuous rate of change of curvature (i.e. G^2 continuity) to be specified at the throat. This was shown to allow improved lip curvature control. Intake B had improved aerodynamic performance at the design point and was less sensitive to changes in massflow and incidence than Intake A which proved the robustness of the HiCST design.

Data statement

Due to commercial confidentiality agreements the supporting data is not available.

Declaration of competing interest

There is no conflict of interest.

Acknowledgements

This project was funded by Innovate UK (Grant number TSB113075).

References

[1] M.H. Straathof, M.J. Van Tooren, M. Voskuijl, B. Koren, Aerodynamic shape parameterisation and optimisation of novel configurations, in: The Aerodynamics of Novel Configurations: Capabilities and Future Requirements. Proceedings of the 2008 Royal Aeronautical Society Annual Applied Aerodynamics Research Conference, London, 27-28 October, 2008, Royal Aeronautical Society, 2008.
[2] V. Braibant, C. Fleury, Shape optimal design using b-splines, Comput. Methods Appl. Mech. Eng. 44 (3) (1984) 247–267.
[3] P. Venkataraman, A New Procedure for Airfoil Definition, 13th Applied Aerodynamics Conference, AIAA Paper 1995-1875-CP, 1995.
[4] J. Lepine, J.-Y. Trepanier, F. Pepin, Wing aerodynamic design using an optimized nurbs geometrical representation, in: The 38th Aerospace Sciences Meeting and Exhibit, No. AIAA-2000-699, Reno, Nevada, 2000.
[5] Y. Liang, X. Cheng, Z. Li, J. Xiang, Multi-objective robust airfoil optimization based on non-uniform rational b-spline (nurbs) representation, Sci. China, Technol. Sci. 53 (10) (2010) 2708–2717.
[6] R.M. Hicks, P.A. Henne, Wing design by numerical optimization, J. Aircr. 15 (7) (1978) 407–412.
[7] S. Kim, J.J. Alonso, A. Jameson, Multi-element high-lift configuration design optimization using viscous continuous adjoint method, J. Aircr. 41 (5) (2004) 1082–1097.
[8] H. Sobieczky, Parametric airfoils and wing (Chapter), in: Notes on Numerical Fluid Mechanics, vol. 68, Vieweg Verlag, 1999, pp. 71–87.
[9] B.M. Kulfan, J.E. Bussoletti, Fundamental parametric geometry representations for aircraft component shapes, in: 11th AIAA/ISSMO Multidisciplinary Analysis and Optimization, AIAA-2006-6948, Renaissance Portsmouth, VA, 2006.
[10] B.M. Kulfan, Universal parametric geometry representation method, J. Aircr. 45 (1) (2008) 142–158.
[11] M. Tyan, N.V. Nguyen, J.-W. Lee, Improving variable-fidelity modelling by exploring global design space and radial basis function networks for aerofoil design, Eng. Optim. 47 (7) (2015) 885–908.
[12] J. Tao, G. Sun, X. Wang, L. Guo, Robust optimization for a wing at drag divergence Mach number based on an improved PSO algorithm, Aerosp. Sci. Technol. 92 (2019) 653–667.
[13] A. Morris, C. Allen, T. Rendall, Aerodynamic shape optimization of a modern transport wing using only planform variations, Proc. Inst. Mech. Eng., G J. Aerosp. Eng. 223 (6) (2009) 843–851.
[14] T. Lassila, G. Rozza, Parametric free-form shape design with pde models and reduced basis method, Comput. Methods Appl. Mech. Eng. 199 (23–24) (2010) 1583–1592.
[15] G. Anderson, M. Aftosmis, M. Nemec, Constraint-based shape parameterization for aerodynamic design, in: 7th International Conference on Computational Fluid Dynamics, Big Island, Hawaii, 2012.
[16] F. Zhu, N. Qin, Intuitive class/shape function parameterization for airfoils, AIAA J. 52 (1) (2013) 17–25.

[17] P. Castonguay, S. Nadarajah, Effect of Shape Parameterization on Aerodynamic Shape Optimization, 45th AIAA Aerospace Sciences Meeting and Exhibit, AIAA Paper 2007-59, 2007.
[18] R. Derksen, T. Rogalsky, Bezier-PARSEC: an optimized aerofoil parameterization for design, Adv. Eng. Softw. 41 (7–8) (2010) 923–930.
[19] I. Goulos, T. Stankowski, D. MacManus, P. Woodrow, C. Sheaf, Civil turbofan engine exhaust aerodynamics: impact of bypass nozzle after-body design, Aerosp. Sci. Technol. 73 (2018) 85–95.
[20] Q. Wang, Q. Zhao, Rotor airfoil profile optimization for alleviating dynamic stall characteristics, Aerosp. Sci. Technol. 72 (2018) 502–515.
[21] N. Vu, J. Lee, Aerodynamic design optimization of helicopter rotor blades including airfoil shape for forward flight, Aerosp. Sci. Technol. 42 (2015) 106–117.
[22] J. Wang, J. Cai, Y. Duan, Y. Tian, Design of shape morphing hypersonic inward-turning inlet using multistage optimization, Aerosp. Sci. Technol. 66 (2017) 44–58.
[23] T.T. Zhang, Z.G. Wang, W. Huang, L. Yan, Parameterization and optimization of hypersonic-gliding vehicle configurations during conceptual design, Aerosp. Sci. Technol. 58 (2016) 225–234.
[24] C. Liu, Y. Duan, J. Cai, J. Wang, Application of the 3D multi-block CST method to hypersonic aircraft optimization, Aerosp. Sci. Technol. 50 (2016) 295–303.
[25] H. Kim, M.-S. Liou, Flow simulation and optimal shape design of n3-x hybrid wing body configuration using a body force method, Aerosp. Sci. Technol. 71 (2017) 661–674.
[26] X. Tang, J. Luo, F. Liu, Aerodynamic shape optimization of a transonic fan by an adjoint-response surface method, Aerosp. Sci. Technol. 68 (2017) 26–36.
[27] R. Christie, A. Heidebrecht, D. MacManus, An automated approach to nacelle parameterisation using intuitive class shape transformation curves, in: ASME Turbo Expo 2016: Turbomachinery Technical Conference and Exposition, vol. 1, American Society of Mechanical Engineers, 2016.
[28] R. Christie, A. Heidebrecht, D. MacManus, An automated approach to nacelle parameterization using intuitive class shape transformation curves, J. Eng. Gas Turbines Power 139 (6) (2017) 062601.
[29] M. Ceze, M. Hayashi, E. Volpe, A study of the CST parameterization characteristics, in: Proceedings of the 27th AIAA Applied Aerodynamics Conference, San Antonio, Texas, 2009, p. 3767.
[30] M. Robinson, Short and Slim Nacelle Design for Ultra-High BPR Engines, 55th AIAA Aerspace Sciences Meeting, AIAA Paper 2017-0708, 2017.
[31] F. Tejero, M. Robinson, D.G. MacManus, C. Sheaf, Multi-objective optimisation of short nacelles for high bypass ratio engines, Aerosp. Sci. Technol. 91 (2019) 410–421.
[32] D. Howe, T. Wynosky, Energy Efficient Engine Program Advanced Turbofan Nacelle Definition Study, Technical Report CR-1/4942, NASA, 1985.
[33] A. Petrusson, Aerodynamic Evaluation of Nacelles for Engines with Ultra High Bypass Ratio, Master's thesis in Applied Mechanics Chalmers University of Technology, Göteborg, Sweden, 2017.
[34] R. Christie, A. Heidebrecht, D. MacManus, Aero-engine installation modelling and the impact on overall flight performance, in: Advanced Aero Concepts, Design and Operations, Royal Aeronautical Society, 2014.
[35] MIDAP Study Group, Agardograph No. 237 Guide to In-Flight thrust Measurement of Turbojets and Fan Engines, Tech. Rep. AG-237, AGARD, 1979.
[36] M. Robinson, D. MacManus, C. Sheaf, Aspects of aero-engine nacelle drag, Proc. Inst. Mech. Eng., G J. Aerosp. Eng. 233 (5) (2019) 1667–1682.
[37] A. Ravankar, A.A. Ravankar, Y. Kobayashi, T. Emaru, Shp: smooth hypocycloidal paths with collision-free and decoupled multi-robot path planning, Int. J. Adv. Robot. Syst. 13 (3) (2016) 133.
[38] ANSYS Inc., 275 Technology Drive, Canonsburg, PA 15317, Fluent User's Guide.
[39] P. Roache, Perspective: a method for uniform reporting of grid refinement studies, J. Fluids Eng. 116 (3) (1994) 405–413.
[40] T.P. Stańkowski, D.G. MacManus, C.T. Sheaf, R. Christie, Aerodynamics of aero-engine installation, Proc. Inst. Mech. Eng., G J. Aerosp. Eng. 230 (14) (2016) 2673–2692.
[41] F. Tejero, D.G. MacManus, C. Sheaf, Surrogate-based aerodynamic optimisation of compact nacelle aero-engines, Aerosp. Sci. Technol. 93 (2019) 105207.
[42] K. Deb, A. Pratap, S. Agarwal, T. Meyarivan, A fast and elitist multiobjective genetic algorithm: NSGA-II, IEEE Trans. Evol. Comput. 6 (2002) 182–197.
[43] A. Heidebrecht, T. Stańkowski, D. MacManus, Parametric geometry and computational process for turbofan nacelles, in: ASME Turbo Expo 2016: Turbomachinery Technical Conference and Exposition, American Society of Mechanical Engineers, 2016.
[44] A.K. Sehra, W. Whitlow Jr., Propulsion and power for 21st century aviation, Prog. Aerosp. Sci. 40 (4–5) (2004) 199–235.
[45] A. Peters, Z.S. Spakovszky, W.K. Lord, B. Rose, Ultrashort nacelles for low fan pressure ratio propulsors, J. Turbomach. 137 (2) (2015) 021001.
[46] J. Murphy, D. MacManus, Inlet ground vortex aerodynamics under headwind conditions, Aerosp. Sci. Technol. 15 (3) (2011) 207–215.
[47] D. Gil-Prieto, D.G. MacManus, P.K. Zachos, A. Bautista, Assessment methods for unsteady flow distortion in aero-engine intakes, Aerosp. Sci. Technol. 72 (2018) 292–304.
[48] C.A. Hall, T.P. Hynes, Measurements of intake separation hysteresis in a model fan and nacelle rig, J. Propuls. Power 22 (4) (2006) 872–879.
[49] K. Lee, B. Lee, S. Kang, S. Yang, D. Lee, Inlet distortion test with gas turbine engine in the altitude engine test facility, in: 27th AIAA Aerodynamic Measurement Technology and Ground Testing Conference, AIAA 2010-4337, 2010.
[50] J.C. Vassberg, M.A. DeHaan, S.M. Rivers, R.A.R.A. Wahls, Development of a Common Research Model for Applied CFD Validation Studies, 26th AIAA Applied Aerodynamics Conference, AIAA Paper 2008-6919, 2008.
[51] P.P. Walsh, P. Fletcher, Gas Turbine Performance, Blackwell Scientific Publications, Oxford, 2004.
[52] S. Farokhi, Aircraft Propulsion, Wiley, New York, 2014.
[53] V. Chandavari, M.S. Palekar, Diffuser angle control to avoid flow separation, Intern. J. Tech. Res. Appl. 2 (5) (2014) 16–21.
[54] ANSYS Inc., 275 Technology Drive, Canonsburg, PA 15317, ICEM CFD User's Manual.
[55] P. Roache, Verification and Validation in Computational Science and Engineering, Hermosa Publishers, 1998.



https://dspace.org/

The use of hybrid intuitive class shape transformation curves in aerodynamic design

Christie, Robert; Robinson, Matthew; Tejero, Fernando; MacManus, David G.

2019-10-23
Elsevier
https://doi.org/10.1016/j.ast.2019.105473
Christie R, Robinson M, MacManus D, Tejero F. (2019) The use of hybrid intuitive class shape transformation curves in aerodynamic design. Aerospace Science and Technology, Volume 95, December 2019, Article number 105473

Downloaded from a DSpace repository. https://dspace.org/